Body-wave interferometry using regional earthquakes with multidimensional deconvolution after wavefield decomposition at free surface

Nori Nakata,[1] Roel Snieder[2] and Michael Behm[3]

[1]*Department of Geophysics, Stanford University, Stanford, CA 94305, USA. E-mail: nnakata@stanford.edu*
[2]*Center for Wave Phenomena, Colorado School of Mines, Golden, CO 80401, USA*
[3]*Department of Meteorology and Geophysics, University of Vienna, Vienna, Austria*

SUMMARY

Passive seismic methods using earthquakes can be applied for extracting body waves and obtaining information of subsurface structure. In this study, we retrieve direct and reflected plane waves by applying seismic interferometry to the recorded ground motion from a cluster of regional earthquakes. We apply upgoing/downgoing *P/S* wavefield decomposition, time windowing, and multidimensional deconvolution to improve the quality of the extraction of reflected waves with seismic interferometry. The wavefield separation and seismic interferometry based on multidimensional deconvolution allow us to reconstruct *PP, PS, SP* and *SS* reflected waves without unwanted crosstalk between *P* and *S* waves. From earthquake data, we obtain *PP, PS* and *SS* reflected plane waves that reflect off the same reflector, and estimate *P*- and *S*-wave velocities.

Key words: Time-series analysis; Spatial analysis; Interferometry; Body waves.

1 INTRODUCTION

Body waves obtained from earthquakes (especially teleseismic events) have been used for imaging deep structure (crust–mantle, e.g. Bostock & Sacchi 1997; Bostock & Rondenay 1999; Baig *et al.* 2005; Dasgupta & Nowack 2006). Receiver-function analysis is one technique to obtain information of subsurface structure by estimating traveltime differences between *P* and *PS* converted waves (e.g. Langston 1979; Li *et al.* 2000; Assumpção *et al.* 2002). Seismic interferometry (Aki 1957; Claerbout 1968; Wapenaar 2004) is also used for analyses of passive seismic waves including earthquake records. One can apply seismic interferometry to body waves generated by earthquakes and obtain images of subsurface structure (e.g. Abe *et al.* 2007; Tonegawa *et al.* 2009; Ruigrok *et al.* 2010; Ruigrok & Wapenaar 2012). Abe *et al.* (2007) found that the image obtained from seismic interferometry has higher resolution than retrieved from receiver functions, but seismic interferometry creates spurious reflectors caused by higher-order multiples and crosstalk between *P* and *S* waves, which can be reduced by averaging over many earthquakes. Higher-resolution Green's functions are also obtained by estimating and deconvolving source functions from earthquake data recorded by a receiver array (Bostock 2004). The target for most body-wave seismic interferometry studies is deep structure, and comparably few studies aim at imaging the shallow crust (Ryberg 2011; Yang *et al.* 2012; Behm & Shekar 2014). Seismic interferometry has been developed for analysing data trace by

trace, and Wapenaar *et al.* (2008a,b) improve seismic interferometry by using multidimensional deconvolution (MDD). Although MDD interferometry requires one to separate wavefields depending on the direction of wave propagation and to solve an inverse problem, MDD overcomes several limitations (e.g. attenuation, complicated incident waves, and source distribution) of trace-by-trace interferometry (see Section 4.3).

In this study, we apply trace-by-trace and MDD seismic interferometry to earthquake data to retrieve direct and reflected plane waves. We first propose a technique of wavefield decomposition at the free surface. Using this decomposition, we separate observed two-component wavefields into upgoing/downgoing *P/S* wavefields, which is necessary for MDD interferometry. Next, we introduce earthquake data observed at the LaBarge field in Wyoming. Then we show a mathematical description of seismic interferometry and step-by-step improvement of interferometric wavefields by applying different techniques to the earthquake data.

2 UPGOING/DOWNGOING *P/S* WAVEFIELD DECOMPOSITION

A number of studies propose different techniques for wavefield separation: using, for example, dual sensors (Loewenthal & Robinson 2000), Helmholtz decomposition (Robertsson & Muyzert 1999; Robertsson & Curtis 2002), over/under towed-streamer acquisition

Table 1. Notations of physical parameters and wavefields.

Notation	Description	Relationship with other parameters
ω	Angular frequency[a]	
α	*P*-wave velocity at the layer below the free surface	
β	*S*-wave velocity at the layer below the free surface	
ρ	Density	
σ_{ij}	Stress in the *ij* component	
μ	Lame's parameters	$\mu = \beta^2 \rho$
λ	Lame's parameters	$\lambda = (\alpha^2 - 2\beta^2)\rho$
θ_p	Angle of the *P* incident wave with respect to the free surface	
θ_s	Angle of the *S* incident wave with respect to the free surface	
k	Horizontal wavenumber	$k = \omega \sin\theta_p/\alpha = \omega \sin\theta_s/\beta$
v_p	Vertical wavenumber for *P* wave	$v_p = \omega \cos\theta_p/\alpha = \sqrt{\omega^2/\alpha^2 - k^2}$
v_s	Vertical wavenumber for *S* wave	$v_s = \omega \cos\theta_s/\beta = \sqrt{\omega^2/\beta^2 - k^2}$
u_z	Vertical component of the displacement of observed wavefields	
u_x	Horizontal component of the displacement of observed wavefields	
$\boldsymbol{U_p}$	Vector displacement of upgoing *P* waves	
$\boldsymbol{D_p}$	Vector displacement of downgoing *P* waves	
$\boldsymbol{U_s}$	Vector displacement of upgoing *S* waves	
$\boldsymbol{D_s}$	Vector displacement of downgoing *S* waves	
U_p	Scalar displacement of upgoing *P* waves at the free surface	
D_p	Scalar displacement of downgoing *P* waves at the free surface	
U_s	Scalar displacement of upgoing *S* waves at the free surface	
D_s	Scalar displacement of downgoing *S* waves at the free surface	
U_p^d	Direct upgoing *P* waves	
U_p^r	Surface-related reflected upgoing *P* waves	$U_p = U_p^d + U_p^r$
G	Green's function	

[a]We consider that the angular frequency is positive; therefore vertical wavenumbers are also positive. For negative frequencies, we compute complex conjugate of a function in positive frequencies (with flipped wavenumbers for the wavenumber–frequency domain).

(Moldoveanu *et al.* 2007) and two steps of acoustic and elastic decomposition (Schalkwijk *et al.* 2003). Dankbaar (1985) proposed a filter to separate upgoing *P* and *SV* waves from multicomponent seismic records. Wavefield separation improves wavefields obtained from interferometry to focus on target reflections (Mehta *et al.* 2007; Vasconcelos *et al.* 2008; van der Neut & Bakulin 2009). When receivers are embedded in a medium (e.g. ocean-bottom and borehole sensors), observed wavefields can be decomposed based on the direction of the wave propagation. Therefore, one can restrict the radiation pattern of virtual sources to suppress some spurious reflections caused by incomplete data acquisition for seismic interferometry (Mehta *et al.* 2007). Because receivers are deployed at the free surface in our data, we cannot suppress the spurious multiples by separating wavefields based on the direction of wave propagation. We employ time windows to reduce the spurious multiples (Bakulin & Calvert 2006), and apply wavefield decomposition for separating the direction of wave propagation, which is necessary for MDD (Wapenaar *et al.* 2011b) and for suppressing crosstalk of *P* and *S* waves.

We decompose wavefields into upgoing/downgoing *P/S* waves using the stress-free boundary condition at the free surface (similar to Wapenaar *et al.* 1990). Table 1 shows the notation used in this study, and Fig. 1 defines the positive directions of *x*, *z* and each wavefield. We consider an isotropic medium and a reflection at the free surface within the vertical plane in which the wave propagates. The goal of this wavefield decomposition is to independently compute U_p, D_p, U_s and D_s from observed data. We assume that a layer below the free surface is laterally homogeneous, which means α and β are constant at the near surface. Based on the theory in Aki & Richards (2002, table 5.1), the displacements of upgoing/downgoing *P/S* waves in the space–time domain using the
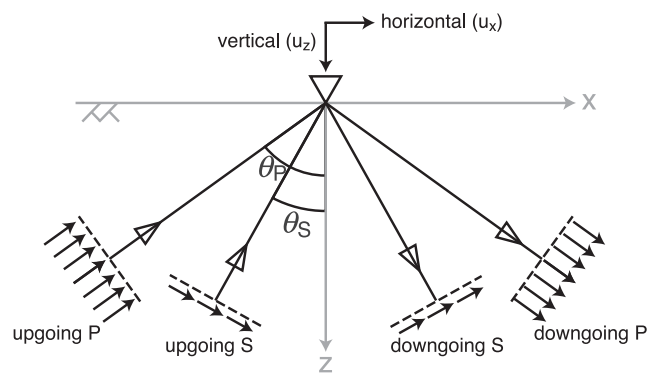
Figure 1. Plane-wave reflection system and coordinates for the wavefield decomposition in Section 2. The horizontal grey line shows the free surface (indicated by ⋌⋋), and the downward triangle on the line is a receiver. The black arrows near the receiver define the positive directions of observed records. The dashed lines illustrate portions of upgoing/downgoing *P/S* plane wave fronts. The black arrows near the dashed lines describe the positive directions of each vector wavefield. Solid black lines connected to dashed lines indicate the ray paths of each wavefield, and the triangles on the solid lines the direction of propagation. The angles θ_P and θ_S are the angles of incidence for *P* and *S* waves, respectively.

Fourier convention $f(x, t) = (1/2\pi)^2 \iint_{-\infty}^{\infty} F(k, \omega) e^{i(kx - \omega t)} \, dk \, d\omega$ are given by

$$\boldsymbol{U}_p(x, z, t) = \left(\frac{1}{2\pi}\right)^2 \iint_{-\infty}^{\infty} U_p(k, \omega) \frac{\alpha}{\omega} \begin{pmatrix} k \\ -v_p \end{pmatrix} e^{i(kx - v_p z - \omega t)} dk \, d\omega,$$

$$\boldsymbol{D}_p(x, z, t) = \left(\frac{1}{2\pi}\right)^2 \iint_{-\infty}^{\infty} D_p(k, \omega) \frac{\alpha}{\omega} \begin{pmatrix} k \\ v_p \end{pmatrix} e^{i(kx + v_p z - \omega t)} dk \, d\omega,$$

$$\boldsymbol{U}_s(x, z, t) = \left(\frac{1}{2\pi}\right)^2 \iint_{-\infty}^{\infty} U_s(k, \omega)\frac{\beta}{\omega}\begin{pmatrix} \nu_s \\ k \end{pmatrix} e^{i(kx - \nu_s z - \omega t)}\, dk\, d\omega,$$

$$\boldsymbol{D}_s(x, z, t) = \left(\frac{1}{2\pi}\right)^2 \iint_{-\infty}^{\infty} D_s(k, \omega)\frac{\beta}{\omega}\begin{pmatrix} \nu_s \\ -k \end{pmatrix} e^{i(kx + \nu_s z - \omega t)}\, dk\, d\omega,$$

$$(1)$$

where the subscript s denotes *SV* waves. Since the scalar displacements are composed of constant amplitudes of upgoing waves and reflection coefficients at the free surface (see table 5.1 in Aki & Richards 2002), these scalar displacements are functions of wavenumber and frequency but not of depth. In the wavenumber–frequency domain, expression (1) is written as:

$$\boldsymbol{U}_p(k, z, \omega) = U_p(k, \omega)\frac{\alpha}{\omega}\begin{pmatrix} k \\ -\nu_p \end{pmatrix} e^{-i\nu_p z},$$

$$\boldsymbol{D}_p(k, z, \omega) = D_p(k, \omega)\frac{\alpha}{\omega}\begin{pmatrix} k \\ \nu_p \end{pmatrix} e^{i\nu_p z},$$

$$\boldsymbol{U}_s(k, z, \omega) = U_s(k, \omega)\frac{\beta}{\omega}\begin{pmatrix} \nu_s \\ k \end{pmatrix} e^{-i\nu_s z},$$

$$\boldsymbol{D}_s(k, z, \omega) = D_s(k, \omega)\frac{\beta}{\omega}\begin{pmatrix} \nu_s \\ -k \end{pmatrix} e^{i\nu_s z}.$$

$$(2)$$

From expression (2), the horizontal and vertical components of the displacement are, in the wavenumber–frequency domain, given by:

$$u_x(k, z, \omega) = U_p(k, \omega)\frac{\alpha k}{\omega}e^{-i\nu_p z} + D_p(k, \omega)\frac{\alpha k}{\omega}e^{i\nu_p z}$$
$$+ U_s(k, \omega)\frac{\beta \nu_s}{\omega}e^{-i\nu_s z} + D_s(k, \omega)\frac{\beta \nu_s}{\omega}e^{i\nu_s z}, \qquad (3)$$

$$u_z(k, z, \omega) = U_p(k, \omega)\frac{-\alpha \nu_p}{\omega}e^{-i\nu_p z} + D_p(k, \omega)\frac{\alpha \nu_p}{\omega}e^{i\nu_p z}$$
$$+ U_s(k, \omega)\frac{\beta k}{\omega}e^{-i\nu_s z} + D_s(k, \omega)\frac{-\beta k}{\omega}e^{i\nu_s z}. \qquad (4)$$

When receivers are located at the free surface ($z = 0$), expressions (3) and (4) simplify to

$$u_x(k, 0, \omega) = \frac{1}{\omega}[\alpha k\{U_p(k, \omega) + D_p(k, \omega)\} + \beta \nu_s\{U_s(k, \omega)$$
$$+ D_s(k, \omega)\}], \qquad (5)$$

$$u_z(k, 0, \omega) = \frac{1}{\omega}[-\alpha \nu_p\{U_p(k, \omega) - D_p(k, \omega)\} + \beta k\{U_s(k, \omega)$$
$$- D_s(k, \omega)\}]. \qquad (6)$$

Because the stress condition at the free surface is

$$\sigma_{xz} = 0 \rightarrow \frac{\partial u_x}{\partial z} + \frac{\partial u_z}{\partial x} = 0, \qquad (7)$$

$$\sigma_{zz} = 0 \rightarrow \lambda\left(\frac{\partial u_x}{\partial x} + \frac{\partial u_z}{\partial z}\right) + 2\mu\frac{\partial u_z}{\partial z} = 0, \qquad (8)$$

the scalar displacements satisfy

$$2\alpha k\nu_p\{U_p(k, \omega) - D_p(k, \omega)\}$$
$$- \beta(k^2 - \nu_s^2)\{U_s(k, \omega) - D_s(k, \omega)\} = 0, \qquad (9)$$

$$\alpha(\lambda k^2 + \lambda \nu_p^2 + 2\mu \nu_p^2)\{U_p(k, \omega) + D_p(k, \omega)\}$$
$$- 2\beta \mu k\nu_s\{U_s(k, \omega) + D_s(k, \omega)\} = 0, \qquad (10)$$

where we inserted eqs (3) and (4) into eqs (7) and (8). To solve four unknowns (U_p, D_p, U_s and D_s), we have four equations (eqs 5, 6, 9 and 10); therefore we can compute scalar wavefields:

$$U_p(k, \omega) = \frac{\beta^2 k}{\alpha\omega}u_x(k, 0, \omega) - \frac{\omega^2 - 2\beta^2 k^2}{2\alpha\omega\nu_p}u_z(k, 0, \omega),$$

$$D_p(k, \omega) = \frac{\beta^2 k}{\alpha\omega}u_x(k, 0, \omega) + \frac{\omega^2 - 2\beta^2 k^2}{2\alpha\omega\nu_p}u_z(k, 0, \omega),$$

$$U_s(k, \omega) = \frac{\omega^2 - 2\beta^2 k^2}{2\beta\omega\nu_s}u_x(k, 0, \omega) + \frac{\beta k}{\omega}u_z(k, 0, \omega),$$

$$D_s(k, \omega) = \frac{\omega^2 - 2\beta^2 k^2}{2\beta\omega\nu_s}u_x(k, 0, \omega) - \frac{\beta k}{\omega}u_z(k, 0, \omega). \qquad (11)$$

Finally, we apply inverse Fourier transforms to expression (11) to obtain upgoing/downgoing *P/S* waves in the space–time domain. Depending on the data, the upcoming *P* and *S* waves may be very weak for specific wavenumbers and frequencies. As shown in the Appendix, eq. (11) is valid even when $U_p(k, \omega) = 0$ or $U_s(k, \omega) = 0$.

If we knew k, θ_p and θ_s, we could solve eq. (11) with one receiver in the space–time domain; however, the estimation is difficult because incoming waves are composed of a variety of angles of incidence. Therefore for this decomposition, we need a receiver array for the Fourier transform, which decomposes the wavefields into the different wavenumber components k and the assumption, in which velocities just below the free surface in the region of this array are constant (laterally homogeneous in the near surface). In expression 11, u_x and u_z are observed wavefields after a double Fourier transform, k and ω are given in the wavenumber–frequency domain, and ν_p and ν_s can be computed in the wavenumber–frequency domain when α and β are given (Table 1). In conclusion, when we assume α and β, we can compute U_p, D_p, U_s and D_s using eq. (11).

To estimate velocities, we use the fact that U_p and U_s do not include direct *S* and *P* waves, respectively. If we use correct velocities, the amplitudes of the direct *P* waves in U_s are zero and those of direct *S* waves in U_p are also zero. Therefore, we can estimate α and β by minimizing amplitudes around arrival times of direct *P* waves in U_s and of direct *S* waves in U_p. Note that because U_s only depends on β (see eq. 11), the estimation of β from U_s and then α from U_p is computationally easier.

3 EARTHQUAKE DATA

3.1 Data set and previous studies

We analyse local earthquake data recorded at the LaBarge field in Wyoming (Fig. 2) to extract subsurface information using seismic interferometry. A dense receiver network, which contained 55 three-component broad-band seismometers with a 250-m average receiver interval, recorded more than 200 regional earthquakes (Fig. 3) during a continuous recording period (2008 November–2009 June). With the dense receiver geometry, we have an opportunity to obtain relatively shallow structural information ($\lesssim$5 km). Based on the earthquake catalog provided by U.S. Geological Survey (USGS) and the EarthScope Array Network Facility (ANF), the magnitudes and depths of almost all observed earthquakes are smaller than 2 and shallower than 10 km, respectively.

Using this data set, several studies obtain images and/or velocities of the subsurface in the survey area. Leahy *et al.* (2012) apply receiver function to teleseismic events to image the subsurface.
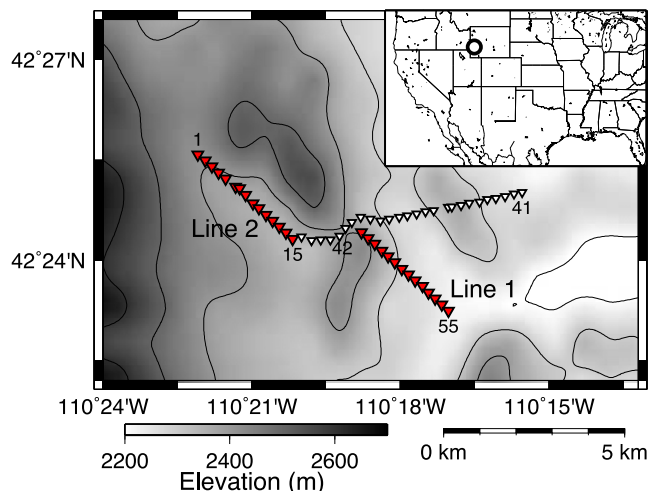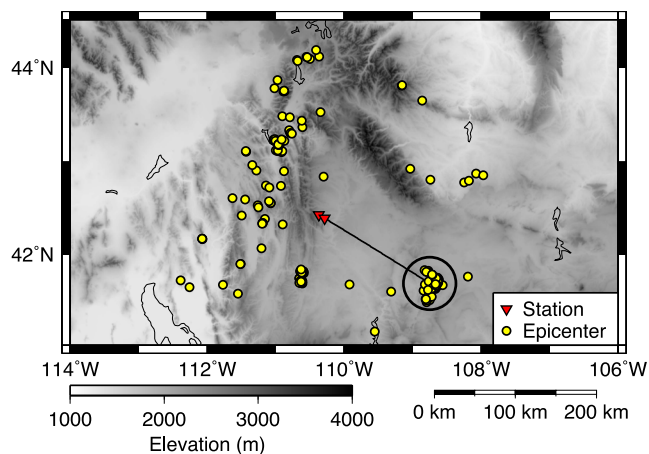
Figure 2. Geometry of receivers (triangles). We use receivers shown by red triangles for this study. Survey lines 1 and 2 contain receivers 1–15 and 42–55, respectively. The circle on the inset shows the location of the magnified area. The grey scale illustrates topography.

Schmedes *et al.* (2012) and Biryol *et al.* (2013) apply earthquake tomography to teleseismic and local earthquake data, respectively. Behm *et al.* (2014) apply seismic interferometry to reconstruct surface waves using traffic-induced noise and obtain Rayleigh- and Love-wave velocities. With teleseismic data, Behm & Shekar (2014) obtain shallow images from vertically incident reflected waves by employing blind deconvolution.

3.2 Observed data

Because the wavefield decomposition in Section 2 is valid for the wave propagation in a vertical plane, we restrict ourselves to hypocentres and receivers near the vertical plane. We use a cluster of earthquakes (represented by the black circle in Fig. 3), which contains about 100 earthquakes and produces quasi-plane waves with nearly the same angles of incidence. This cluster of earthquakes is 180 km away from the stations and located on the extensions of sur-


Figure 3. Geometry of earthquakes (yellow dots) and receivers (red triangles). We use an earthquake cluster (embraced by black circle) for the interferometry study. Triangles indicate the locations of receivers No. 1 and 55. The black line illustrates the great circle between the centre of the earthquake cluster and receiver No. 55. The grey scale illustrates topography.
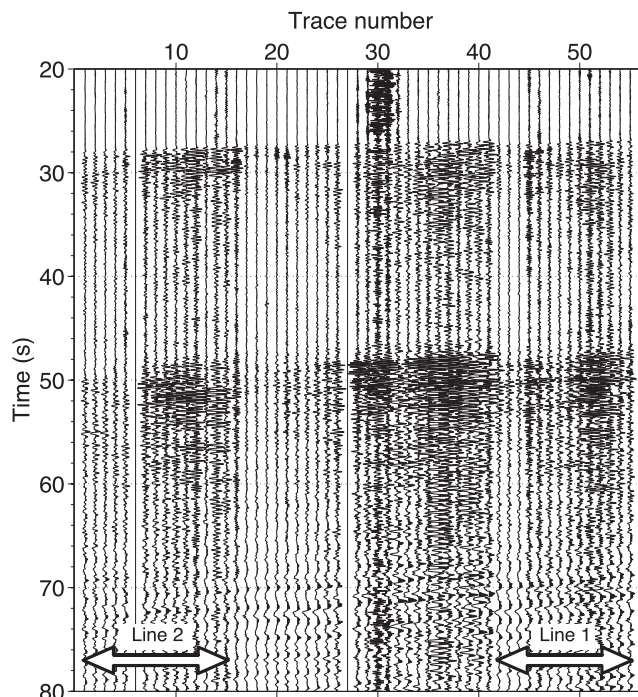
Figure 4. Example of observed records from an earthquake in the north–south horizontal component after applying a bandpass filter, 0.4–0.5–7–9 Hz. Time 0 s is the origin time of the earthquake. Trace numbers correspond with the receiver numbers in Fig. 2. The white arrows show the receivers used for survey lines 1 and 2.

vey lines 1 and 2 in Fig. 2 (see the black line in Fig. 3). Therefore in this study, we use this cluster of earthquakes and receivers of survey lines 1 and 2 (the red triangles in Fig. 2) to reconstruct direct and reflected plane waves with seismic interferometry.

Fig. 4 shows sample observed wavefields excited by one earthquake. Direct *P* waves arrive around 28 s, *S* waves around 50 s, and surface waves around 70 s. Wavefields at receivers 29–30 are contaminated by traffic noise which is generated from a road close to these receivers. The high-energy waveforms contain frequencies up to 7 Hz. Because the aperture of the receiver array is small, we cannot accurately interpret seismic phases of each arriving wave from the move out of traveltimes in Fig. 4. Seismic phases of incoming waves comprise refracted waves from the crust (*Pg*, *Sg*), reflected waves from the crust-mantle boundary (Moho) (*PmP*, *SmS*), and refracted waves from the uppermost mantle (*Pn*, *Sn*). Note that we can apply seismic interferometry to any types of phases and we do not have to specify the seismic phases because we are interested in reflected waves from the shallow crust below the receiver array, and all seismic phases can produce these waves. Some studies use specific seismic phases to confine the angle of incident waves (e.g. Ruigrok *et al.* 2010; Ruigrok & Wapenaar 2012). In this study, we estimate the traveltimes of each seismic phase to validate our interferometric wavefields, where we evaluate whether the reconstructed waves with seismic interferometry are reflected waves or later phases. To estimate traveltimes and relative amplitudes of each phase, we construct a local 3-D subsurface model based on Gans (2011) that includes crustal inhomogeneity and perform 3-D ray tracing with the program ANRAY (Pšenčík 1998). Results from ray tracing suggest that traveltime differences are very small for *Pn*/*Pg* as well as *Sn*/*Sg*, and *PmP*/*SmS* arrive 0.7/1.2 s later than *Pn*/*Sn*. At this offset, amplitudes of *Pg*/*Sg* are smaller than *Pn*/*Sn*
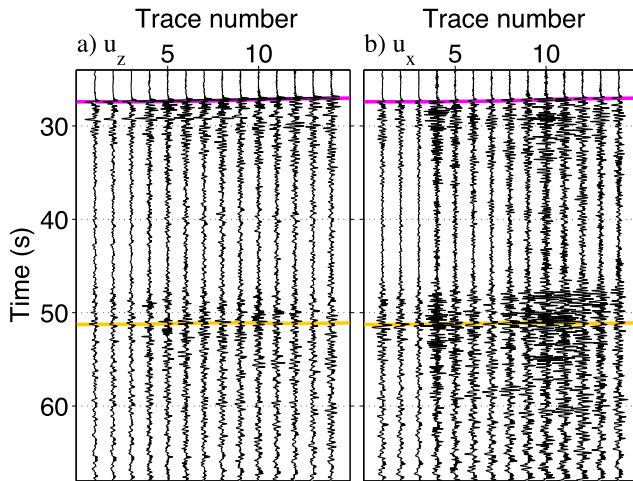
Figure 5. Space-interpolated observed record in (a) vertical and (b) radial components in line 1 (after rotating the horizontal components into the radial direction) from the same earthquake used in Fig. 4. Trace number is assigned after the space interpolation, and traces 1–14 correspond to receivers 42–55 in Fig. 4. We apply the same bandpass filter used in Fig. 4 to waveforms in all panels. The pink and yellow lines indicate the picked arrival times for the largest energy of direct *P* and *S* waves, respectively. Amplitudes are normalized individually at each panel.

and *PmP/SmS*. Although both traveltimes and, in particular, amplitudes still depend on the subsurface model, we conclude that the observed first arrivals are most likely *Pn/Sn* or *PmP/SmS* since their amplitudes are expected to be stronger than amplitudes of *Pg/Sg* waves.

3.3 Wavefield decomposition

To apply wavefield decomposition in the wavenumber–frequency domain using eq. (11), we need traces at uniform spatial intervals. Therefore, we interpolate the observed data in space using a spline interpolation before the decomposition. Note that the receiver intervals in survey lines 1 and 2 are almost uniform and the interpolation distances are small. Fig. 5 shows the interpolated wavefields after rotating the horizontal components in the radial direction (the same direction as the receiver lines).

Fig. 6 shows the particle motion around the *P*- and *S*-wave arrival times. We compute the angles of incident *P* and *S* waves by ray tracing with a velocity model based on Gans (2011); the angles of incidence in survey line 1 are 35° and 18° for *P* and *S* waves, respectively (the blue lines in Fig. 6). The particle motions around the *P*-wave arrivals correspond to the angle of incidence estimated by ray tracing, but the particle motions around *S*-wave arrivals do not. These particle motions do not show a clear pattern, which may be caused by the fact that *S* waves overlap with the *P*-wave coda, the *S*-wave arrival time is less clear than the *P*-wave time (see Fig. 5), and the subsurface may create strong PS converted waves (which we discuss later). Note that in both *P* and *S* waves, the particle motions do not have to perfectly align to the angle of incidence estimated by ray tracing because the incoming waves are not perfect plane waves and the velocity model for the ray tracing has some uncertainties.

Wavefield decomposition shown in eq. (11) requires *P*- and *S*-wave velocities. We do not need to know the angle of incidence for the wavefield decomposition because we solve eq. (11) in the wavenumber–frequency domain. To estimate velocities, we employ the method proposed in Section 2 and minimize upgoing
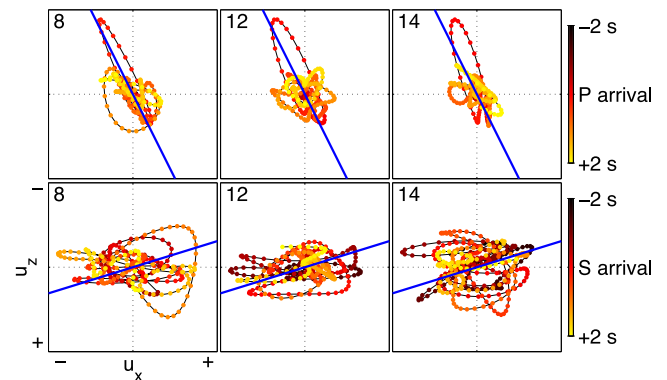

Figure 6. Particle motion of observed wavefields in the vertical and radial components (Fig. 5) at around (top row) *P*- and (bottom row) *S*-wave arrivals after applying the same bandpass filter used in Fig. 4. Red (0 s in the colour bar) indicates the times at the pink line for *P* waves and the yellow line for *S* waves in Fig. 5. Blue lines illustrate the particle motion based on the angle of incidence estimated by ray tracing. Top-left numbers at each panel describe trace numbers of each motion.

P-wave amplitude around *S*-wave arrival times as well as upgoing *S*-wave amplitude around *P*-wave arrival times. Fig. 7 shows upgoing/downgoing *P/S* waves decomposed from waves in Fig. 5 with estimated *P*- and *S*-wave velocities, which are 3.5 and 1.2 km s⁻¹, respectively. Based on these velocities and an angle of 35° of the *P* incident wave, the reflection coefficients at the free surface are −0.905 (ṖṖ), 0.665 (ṖŚ), 0.273 (ŚṖ) and 0.905 (ŚŚ) (Aki & Richards 2002). In Fig. 7(a), the amplitudes in the pink/blue time intervals are larger than the yellow/green time intervals. In contrast in Fig. 7(b), amplitude differences between the pink/blue and yellow/green time intervals are not clear, which implies that the wavefields include strong PS converted waves in the pink/blue time interval.

Figs 8 and 9 show comparisons of wavefields and particle motions between upgoing *P* and *S* waves. In Fig. 8(a), because direct *P* waves (at around 27–27.5 s) exist only in the upgoing *P* wavefields, we successfully separate observed waves into upgoing *P* and *S* waves (see also the top row of Fig. 9). Strong upgoing *S* waves appearing just after the direct *P* waves in Fig. 8(a) indicate that the observed waveforms include strong PS converted waves. Since Fig. 8(b) is mostly red, upgoing *S* wavefields are dominant in this time interval, which implies that we can also separate wavefields in this interval. The particle motions in the bottom row of Fig. 9 are aligned along the horizontal blue lines, which denote that upgoing *S* wavefields are dominant in this interval. The anomalous particle motion in trace 14, which is at the edge of the array, may be caused by the space–wavenumber Fourier transform; therefore, we only use traces 3–12 for interferometry.

4 APPLICATION OF SEISMIC INTERFEROMETRY TO EARTHQUAKE DATA

We introduce a mathematical description of seismic interferometry related to this study while assuming 2-D wave propagation and show reconstructed waveforms from the earthquake data. More information for seismic interferometry is given by Snieder *et al.* (2009) and Wapenaar *et al.* (2010a,b, 2011b), who summarize trace-by-trace and multi-dimensional interferometry. In this section, all equations are written in the space-frequency domain.
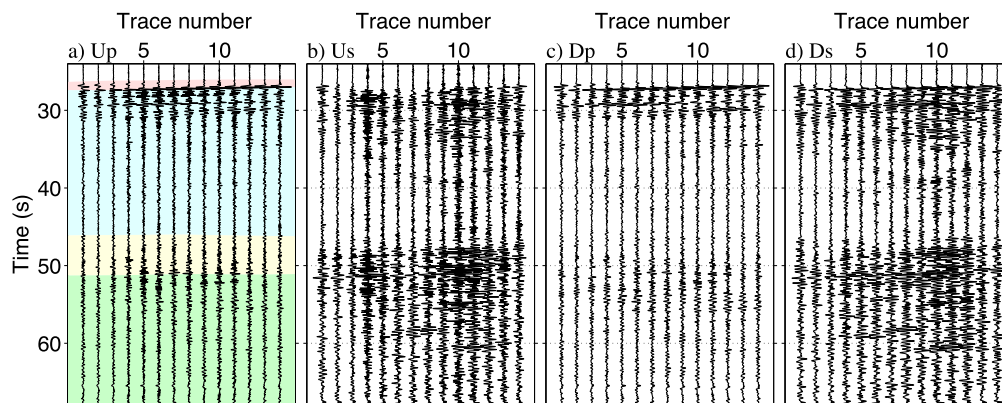
Figure 7. Upgoing/downgoing *P/S* waves after applying wavefield decomposition (eq. 11) to the wavefields in Fig. 5. We employ the same bandpass filter used in Fig. 4 in all panels. The colours in panel (a) indicate the time windows we use in this study to separate direct (pink for *P* and yellow for *S*) and reflected waves (blue for *P* and green for *S*). The arrival times represented by the pink and yellow lines in Fig. 5 locate the interfaces between pink/blue and yellow/green, respectively. Amplitudes are normalized separately at each panel.
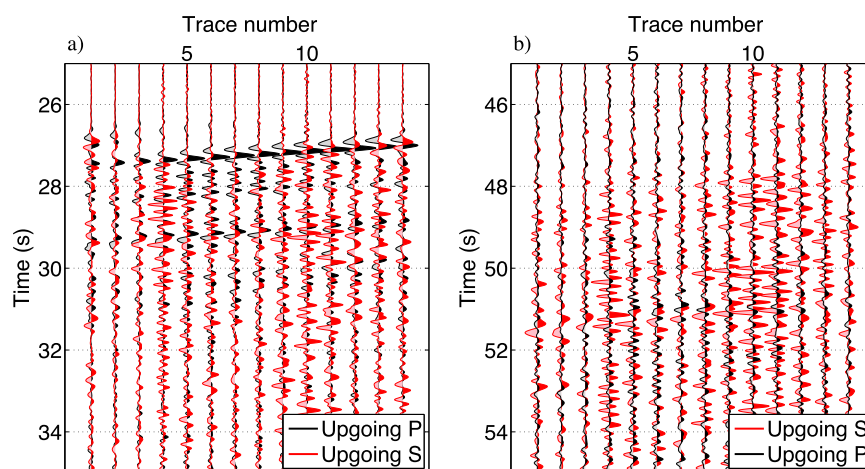
Figure 8. Comparison between upgoing *P* and *S* wavefields in Figs 7(a) and (b) at around (a) *P*-wave and (b) *S*-wave arrival times. Although in both panels upgoing *P* and *S* waves are shown in black and red, respectively, we change the order of wavefields for a display purpose; upgoing *P* is back and upgoing *S* is front in panel (a) and vice versa in panel (b). Amplitude ratios between upgoing *P/S* waves are preserved.

4.1 Trace-by-trace deconvolution

For trace-by-trace deconvolution interferometry, we compute deconvolution for each pair of traces at each earthquake. This method works well in the case of 1-D wave propagation (Snieder & Şafak 2006; Nakata & Snieder 2012) and can be applied to higher dimensions (e.g. Vasconcelos & Snieder 2008b).

4.1.1 Deconvolution without wavefield decomposition

Deconvolution applied to the waveforms from one earthquake recorded by the vertical component of receivers *A* and *B* is given by

$$DI_{zz}(B, A) = \frac{u_z(B)}{u_z(A)} \approx \frac{u_z(B)u_z^*(A)}{|u_z(A)|^2 + \epsilon \langle |u_z(A)|^2 \rangle}, \quad (12)$$

where ϵ is a regularization parameter (Clayton & Wiggins 1976), the asterisk denotes the complex conjugate, and $\langle \ldots \rangle$ indicates the average power spectrum. In deconvolution interferometry, the receiver at the denominator in eq. (12) (receiver A) behaves as a virtual source (Vasconcelos & Snieder 2008a). We can compute deconvolution for all combinations of the vertical and horizontal

components, and each combination corresponds to different types of wave propagation between receivers *A* and *B*. For simplicity, we show only one combination in eq. (12). In the 1-D case, $DI_{zz}(B, A)$ is equivalent to the wave propagation from receiver *A* to receiver *B* (Snieder *et al.* 2006). In the 2-D and 3-D cases, we average $DI_{zz}(B, A)$ over many sources around the receivers to reconstruct the wave propagation (Vasconcelos & Snieder 2008a). Because u_z includes both *P* and *S* waves (see eq. 5), $DI_{zz}(B, A)$ contains crosstalk between *P* and *S* waves.
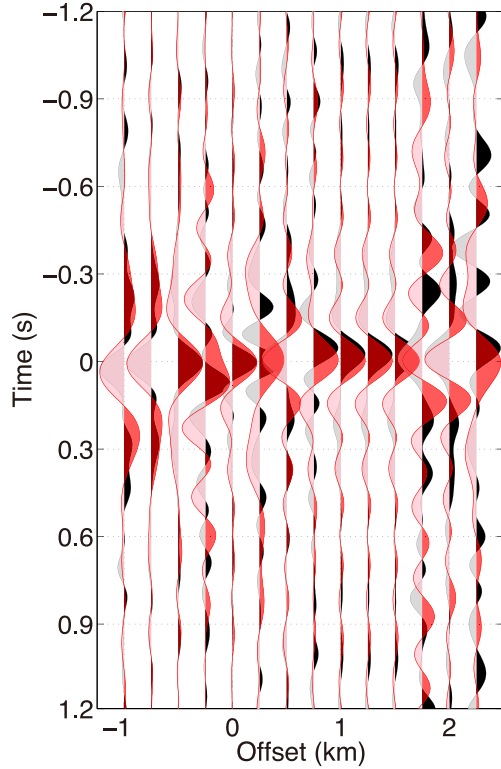
In Fig. 10, we show averaged deconvolved wavefields over all earthquakes after applying trace-by-trace deconvolution to observed wavefields (eq. 12). Receiver A in eq. (12) is at offset 0 km (virtual source). The deconvolved wavefields in Fig. 10 are contaminated by noise around the zero-lag time; hence, trace-by-trace deconvolution using neither wavefield decomposition nor time windowing does not provide useful information about the subsurface.

4.1.2 Direct-wave extraction

To improve interferometric wavefields, we decompose u_x and u_z into U_p, D_p, U_s and D_s (Fig. 7) using eq. (11) before applying seismic interferometry. We represent the wavefield U_p at receiver *B* (the red
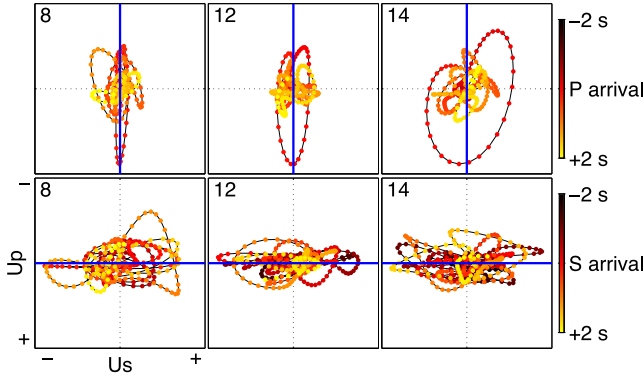
Figure 9. Particle motion of upgoing *P* and *S* wavefields at around (top row) *P*- and (bottom row) *S*-wave arrivals after applying the same bandpass filter used in Fig. 4. Red (0 s in the colour bar) indicates the times at the pink line for *P* wave and the yellow line for *S* waves in Fig. 5. Blue lines illustrate the ideal particle motion of *P* (top row) and *S* (bottom row) waves in the case when wavefields are perfectly separated and no converted waves are generated. Top-left numbers at each panel describe trace numbers of each motion. Note that in contrast to Fig. 6, the axes denote the upgoing *P*- and *S*-wave components.

Figure 11. Schematic plane-wave propagation. Receivers (triangles) are deployed at the free surface (indicated by ⋏⋏), and a plane wave (the black arrow at lower-left) propagates with angle θ of the incidence. Dashed lines, all of which are parallel, indicate the portions of plane waves. The red arrow illustrates the ray path for the different portion of the same plane wave as the black arrow. The model contains one horizontal layer and a half space below the layer. The thickness of the layer is *h*. Grey lines and receivers show unfolded imaginary layers and receivers to understand reflected plane waves based on Snell's law. Distance h_d corresponds with the difference of the travel distance between direct upgoing waves to receivers *A* and *B*, and h_r is the travel distance of the reflected waves from *A* to *B*. We do not show converted waves in this figure.
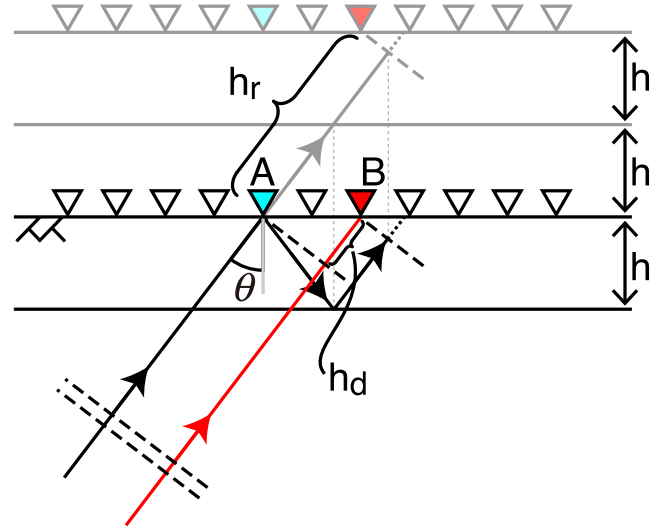

Figure 10. Wavefields at line 1 obtained by applying trace-by-trace deconvolution to observed vertical (black) and radial (red) components (eq. 12). We apply a bandpass filter 0.4–0.5–7–9 Hz to wavefields in the vertical component and 0.4–0.5–4–6 Hz to wavefields in the radial component. Offset 0 km is the location of the virtual source.

the propagation of the direct waves from receiver *A* to receiver *B* (when the waves are plane waves, the Green's function relates to the distance h_d in Fig. 11). Deconvolving eq. (13) with $U_p(A)$ gives G_p:
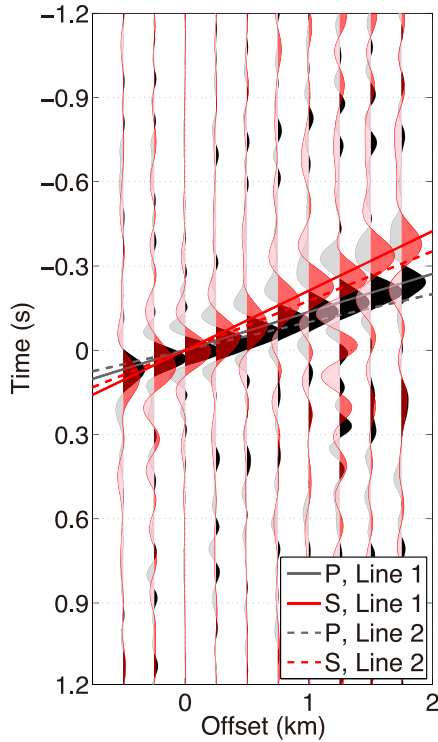
$$\frac{U_p(B)}{U_p(A)} = G_p. \tag{14}$$

In practice, for computing this deconvolution, we use a regularization parameter introduced in eq. (12).

We apply trace-by-trace deconvolution (eq. 14), where we compute $U_p(B)/U_p(A)$ and $U_s(B)/U_s(A)$, to decomposed wavefields obtained from each earthquake and average over all earthquakes used (Fig. 12). The solid lines in Fig. 12 show the dips which maximize the amplitudes of slant-stacked waveforms. These dips depend on the angles of incidence and the wave velocities. Based on the angles of incidence estimated by ray tracing (35° for *P* waves and 18° for *S* waves), the *P*- and *S*-wave velocities are 4.2 and 1.5 km s⁻¹, respectively. These velocities are average velocities over ray paths of the direct waves (h_d in Fig. 11). We also apply this deconvolution to survey line 2 (dashed lines in Fig. 12). The dips in line 2 are flatter than in line 1, which corresponds to a high-velocity layer under line 2 (Leahy *et al.* 2012). Note that without wavefield separation, we cannot clearly reconstruct direct waves (compare Fig. 10 with Fig. 12). The wavefield separation plays an important role for reconstructing waveforms with seismic interferometry.

4.1.3 Reflected-wave extraction

Eq. (13) indicates the relationship between upgoing waves recorded at different receivers. Next, we retrieve the reflected waves (related

triangle in Fig. 11) with the wavefield U_p at receiver *A* (the blue triangle in Fig. 11) as

$$U_p(B) = G_p U_p(A), \tag{13}$$

where we assume that all wavefields recorded at receiver *B* are also recorded at receiver *A*. The Green's function G_P accounts for

Figure 12. Wavefields in survey line 1 obtained by applying trace-by-trace deconvolution to upgoing *P* (black) and *S* (red) waves (eq. 14). The solid lines show the dip of *P* (black) and *S* (red) plane waves in survey line 1, and the dashed lines in survey line 2. We apply the same bandpass filters used in Fig. 10. Offset 0 km is the location of the virtual source.
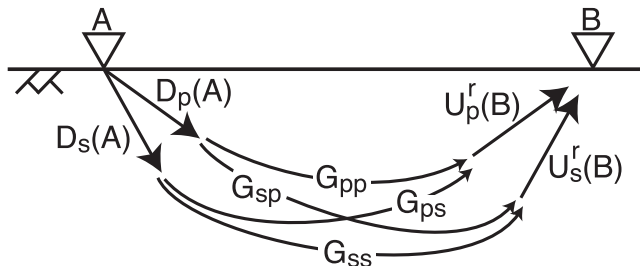
Figure 13. Relationship of upgoing/downgoing *P/S* wavefields and Green's functions between receivers *A* and *B*. The free surface is indicated by ⫣. The direction of arrows represents the direction of causality. Upgoing waves are reflected waves (direct upgoing waves are not shown).

to h_r in Fig. 11) using upgoing and downgoing waves. Surface-related reflected upgoing *P* waves at receiver *B* are given by

$$U_p^r(B) = G_{pp}D_p(A) + G_{ps}D_s(A),\qquad(15)$$

where G_{pp} and G_{ps} are the PP and PS reflected Green's function representing the wave propagation from receiver *A* to receiver *B* (Fig. 13). In this study, we use time windowing to separate direct and reflected waves (see Fig. 7 for an example of time windows). Eq. (15) after deconvolving with $D_p(A)$ is given by

$$\frac{U_p^r(B)}{D_p(A)} = G_{pp} + G_{ps}\frac{D_s(A)}{D_p(A)}.\qquad(16)$$

Although we obtain the PP reflected Green's function (G_{pp}) using eq. (16), the deconvolved wavefield $[U_p^r(B)/D_p(A)]$ is contaminated

by crosstalk of downgoing *P* and *S* waves. Note that we compute $U_p^r(B)/D_p(A)$ to obtain G_{pp}, and $G_{ps}D_s(A)/D_p(A)$ in eq. (16) is an unwanted wave created by crosstalk. Therefore in the elastic-wave case, we cannot obtain pure (no crosstalk) reflected Green's function with trace-by-trace deconvolution.

We compute eq. (16) to obtain PP reflected waves and similar equations for PS, SP and SS reflected waves while applying time windowing for separating direct and reflected waves. We independently create time windows for each earthquake based on manually picking arrivals of each wave, and the time windows shown in Fig. 7(a) are the windows for the earthquake in Fig. 7. When we compute eq. (16) for each earthquake, we use only direct downgoing *P* waves $[D_p^d(A)]$ instead of using entire downgoing waves $[D_p(A)]$ to focus on the first-order surface related multiples as following the technique shown in Mehta *et al.* (2007). With this time window to isolate direct downgoing waves, we may create non-physical reflections caused by insufficient cancellation compared with using the full wavefields (appendix B in Ruigrok 2012). In our data, however, this time-gating technique increases the signal-to-noise ratio of deconvolved wavefields.

Fig. 14 shows all *P/S* combinations of the trace-by-trace deconvolved waveforms after averaging over all earthquakes used. For a display purpose, we show only one receiver gather (at trace 5), but we can compute all combinations of virtual sources and receivers. In Figs 14(a) and (b), we employ the pink/blue time windows shown in Fig. 7(a) (modified for each earthquake), respectively. Similarly, in Figs 14(c) and (d), we use the yellow/green time windows shown in Fig. 7(a) (modified for each earthquake). We apply cosine tapers at the edge of each time window. Although each panel in Fig. 14 aims to show the target reflected Green's function (e.g. G_{pp} for Fig. 14a), each panel includes unwanted crosstalk caused by the last term in eq. (16). Evaluating the amount of crosstalk is difficult, but we expect that the energy of SP reflected waves should be smaller than other reflected waves in the estimated angle of incidence (Aki & Richards 2002); for example in the assumption of horizontal layers, when the *P* and *S* velocities in the first/second layers are 3.5/5.0 and 1.2/2.2 km s^{-1} (modified after Leahy *et al.* 2012) and the angle of *P*-wave incidence is 35°, the reflection coefficients at the interface are 0.189 (ṖṖ), −0.135 (ṖṠ), −0.055 (ṠṖ), and −0.162 (ṠṠ). Almost no *P*-wave energy is present in Fig. 8(b), which also indicates that G_{sp} is small. However, the amplitudes in Fig. 14(c) are larger than those in Fig. 14(d), which might be caused by the crosstalk between downgoing *P* and *S* waves in eq. (16).

The right-most trace at each panel in Fig. 14 shows slant-stacked waveforms, where the dip for stacking (the red lines in Fig. 14) is chosen to maximize the peak amplitude of stacked waveforms. Since the dips are related to the wave velocities and the angles of incidence, the dips in Figs 14(a) and (b) as well as those in Figs 14(c) and (d) are almost the same. Stacked waveforms in Fig. 14 are noisy and difficult to interpret.

4.2 Trace-by-trace cross-coherence

Because normalization in the frequency domain improves the signal-to-noise ratio of interferometric wavefields (Nakata *et al.* 2011), we apply the normalization before deconvolving waveforms, which is so-called cross-coherence interferometry. We normalize eq. (15) with the amplitude of $U_p^r(B)$:

$$\frac{U_p^r(B)}{|U_p^r(B)|} = G_{pp}\frac{D_p(A)}{|U_p^r(B)|} + G_{ps}\frac{D_s(A)}{|U_p^r(B)|}.\qquad(17)$$
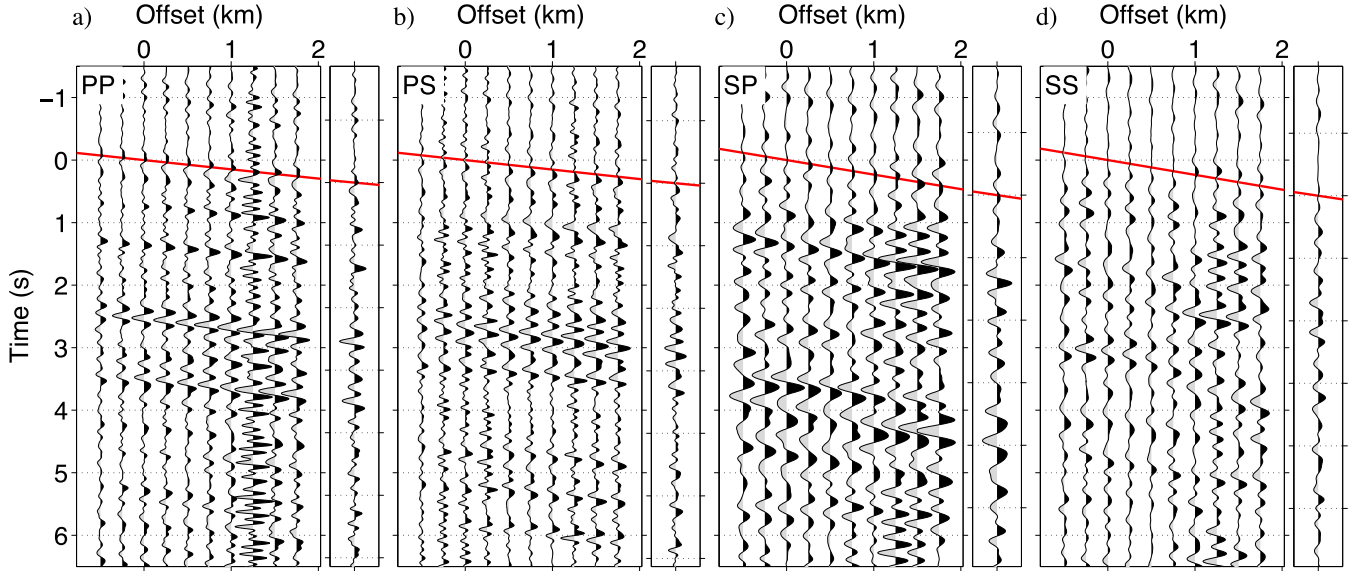
Figure 14. Reflected plane waves retrieved by trace-by-trace deconvolution. We compute (a) $U_p^r(B)/D_p^d(A)$ ($\approx G_{pp}$), (b) $U_p^r(B)/D_s^d(A)$ ($\approx G_{ps}$), (c) $U_s^r(B)/D_p^d(A)$ ($\approx G_{sp}$) and (d) $U_s^r(B)/D_s^d(A)$ ($\approx G_{ss}$). Each panel shows a receiver gather, and offset 0 km indicates the location of the common receiver. We apply bandpass filters with (a, b) 0.4–0.5–7–9 Hz and (c, d) 0.4–0.5–4–6 Hz. Red lines illustrate the dip for slant stacking, and the rightmost trace at each panel is the stacked trace. The amplitudes in panels (c, d) are multiplied by a factor 2.5 compared with those in panels (a, b), and the amplitudes in panels (a, b) are the same.

By deconvolving eq. (17) with $D_p(A)/|D_p(A)|$, we obtain the form of cross-coherence interferometry:

$$\frac{U_p^r(B)}{|U_p^r(B)|}\frac{|D_p(A)|}{D_p(A)} = \frac{U_p^r(B)D_p^*(A)}{|U_p^r(B)||D_p(A)|}$$

$$= \frac{|D_p(A)|}{|U_p^r(B)|}\left\{G_{pp} + G_{ps}\frac{D_s(A)}{D_p(A)}\right\}, \qquad (18)$$

where $|D_p(A)|/|U_p^r(B)|$ is considered as an amplification term. Note that we still have crosstalk between P and S waves in eq. (18) $[G_{ps}D_s(A)/D_p(A)]$. In practice, we use a regularization parameter to compute trace-by-trace cross-coherence (Nakata *et al.* 2013):

$$\frac{U_p^r(B)D_p^*(A)}{|U_p^r(B)||D_p(A)|} \rightarrow \frac{U_p^r(B)D_p^*(A)}{|U_p^r(B)||D_p(A)| + \epsilon\langle|U_p^r(B)||D_p(A)|\rangle}. \qquad (19)$$

When we apply trace-by-trace cross-coherence interferometry to earthquake data, we can suppress noise and compensate amplitude differences among traces by multiplying the term $|D_p(A)|/|U_p^r(B)|$ in eq. (18) as shown by Nakata *et al.* (2011). Fig. 15, in which we also use $D_p^d(A)$ instead of $D_p(A)$, shows more coherent waves than Fig. 14 with the noise in traces around offset 1–1.5 km being suppressed. One criterion to evaluate the quality of the interferometric wavefields is given by using causality. Because we apply time windows, the wavefields after applying interferometry should contain waves only for $t > 0$, and waves for $t < 0$ are noise. Compared Fig. 15 with Fig. 14, the amplitudes in the acausal time in Fig. 15 are smaller than in Fig. 14, which indicates that the wavefields constructed by trace-by-trace cross-coherence have the higher signal-to-noise ratio than trace-by-trace deconvolution. Although cross-coherence improves the signal-to-noise ratio, the waveforms in Fig. 15 include unwanted crosstalk as indicated in eq. (18). For example, a negative-amplitude wave exists at 4.6 s in both stacked waveforms of Figs 15(c) and (d), which may be caused by the crosstalk because *SP* and *SS* waves rarely arrive at the same time.

4.3 Multidimensional deconvolution

In trace-by-trace interferometry, we solve the Green's functions of *P* and *S* reflected waves at each pair of traces for each combination of *P/S* waves separately. In MDD interferometry, we solve the Green's functions of all components for all traces simultaneously. From eq. (15) and the similar notation for *S* waves, we obtain

$$\begin{pmatrix} U_p^r \\ U_s^r \end{pmatrix} = \begin{pmatrix} G_{pp} & G_{ps} \\ G_{sp} & G_{ss} \end{pmatrix}\begin{pmatrix} D_p \\ D_s \end{pmatrix}, \qquad (20)$$

where each wavefield includes all traces [see Fig. 13 to understand eq. (20) schematically]. To solve eq. (20), we first right-multiply $(D_p^\dagger \ D_s^\dagger)$, where † is the complex conjugate transpose (Wapenaar *et al.* 2011b):

$$\begin{pmatrix} U_p^r D_p^\dagger & U_p^r D_s^\dagger \\ U_s^r D_p^\dagger & U_s^r D_s^\dagger \end{pmatrix} = \begin{pmatrix} G_{pp} & G_{ps} \\ G_{sp} & G_{ss} \end{pmatrix}\begin{pmatrix} D_p D_p^\dagger & D_p D_s^\dagger \\ D_s D_p^\dagger & D_s D_s^\dagger \end{pmatrix}, \qquad (21)$$

and then add a damping parameter ϵI to eq. (21) to obtain a stable inverse matrix (van der Neut *et al.* 2011b):

$$\begin{pmatrix} U_p^r D_p^\dagger & U_p^r D_s^\dagger \\ U_s^r D_p^\dagger & U_s^r D_s^\dagger \end{pmatrix}\left\{\begin{pmatrix} D_p D_p^\dagger & D_p D_s^\dagger \\ D_s D_p^\dagger & D_s D_s^\dagger \end{pmatrix} + \epsilon I\right\}^{-1}$$

$$= \begin{pmatrix} G_{pp} & G_{ps} \\ G_{sp} & G_{ss} \end{pmatrix}. \qquad (22)$$

Employing eq. (22), we can retrieve the Green's matrix from upgoing/downgoing *P/S* wavefields.

Because MDD treats the extraction of the Green's function as an inverse problem, MDD has several advantages compared with trace-by-trace interferometry. MDD can be applied to passive seismic data generated by unevenly distributed sources in a dissipative medium (but MDD requires evenly distributed receivers) (van der Neut *et al.* 2011b; Wapenaar *et al.* 2011a,b). Snieder *et al.* (2009) suggest that one can retrieve Green's functions without estimating source spectra by using MDD. This method also removes complicated
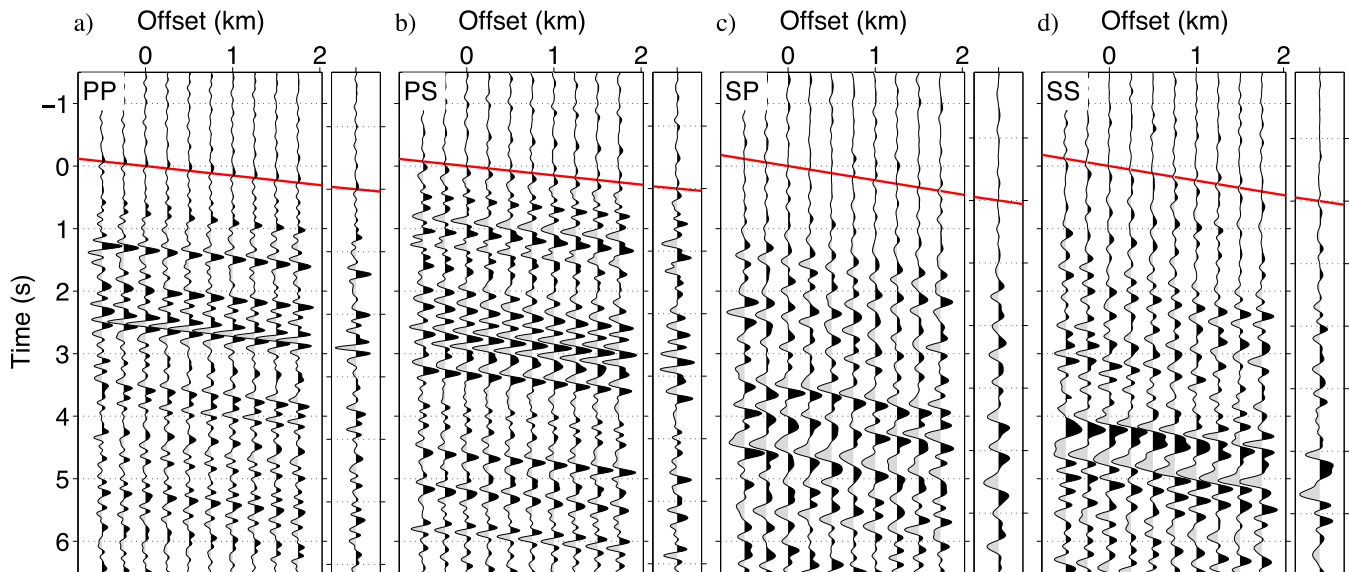
Figure 15. Reflected plane waves retrieved by trace-by-trace cross-coherence. We compute (a) $U_p^r(B)D_p^{d*}(A)/|U_p^r(B)||D_p^d(A)|$ ($\approx G_{pp}$), (b) $U_p^r(B)D_s^{d*}(A)/|U_p^r(B)||D_s^d(A)|$ ($\approx G_{ps}$), (c) $U_s^r(B)D_p^{d*}(A)/|U_s^r(B)||D_p^d(A)|$ ($\approx G_{sp}$) and (d) $U_s^r(B)D_s^{d*}(A)/|U_s^r(B)||D_s^d(A)|$ ($\approx G_{ss}$). Each panel shows a receiver gather, and offset 0 km indicates the location of the common receiver. We apply the same bandpass filters as used in Fig. 14. Red lines illustrate the dip for slant stacking, and the rightmost trace at each panel is the stacked trace. The amplitudes in panels (c, d) are multiplied by a factor 2.5 compared with those in panels (a, b), and the amplitudes in panels (a, b) are the same.
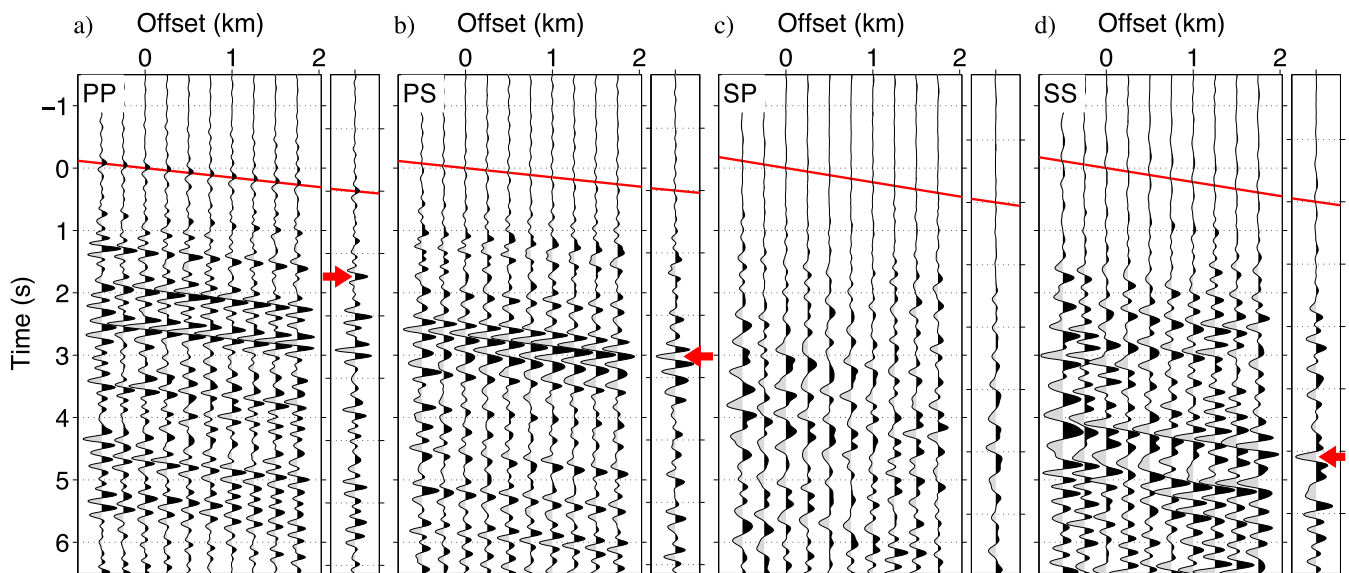
Figure 16. Reflected plane waves retrieved by multidimensional deconvolution. (a) G_{pp}, (b) G_{ps}, (c) G_{sp} and (d) G_{ss}. Each panel shows a receiver gather, and offset 0 km indicates the location of the common receiver. We apply the same bandpass filters as used in Fig. 14. Red lines illustrate the dip for slant stacking, and the rightmost trace at each panel is the stacked trace. The red arrows on the rightmost traces in panels (a, b, d) point at the waves that we interpret. The amplitudes in panels (c, d) are multiplied by a factor 2.5 compared with those in panels (a, b), and the amplitudes in panels (a, b) are the same.

overburden without requiring a velocity model when receivers are embedded inside a medium (van der Neut *et al.* 2011a,b). Note that by comparing eqs (16) and (22), MDD retrieves the Green's functions without unwanted crosstalk when we separate *P* and *S* waves.

Fig. 16 shows wavefields reconstructed by MDD interferometry (expression 22). We again apply time windows to downgoing waves to isolate direct waves for increasing the coherency of deconvolved wavefields. For MDD interferometry, we also have a possibility to create pseudo reflections with applying these time windows (Ruigrok 2012). The amplitudes of the acausal waves are

weaker than those in Figs 14 and 15, which indicates that based on the criterion of causality the quality of wavefields produced by MDD is better than trace-by-trace interferometry. Wavefields in Fig. 16 do not include unwanted crosstalk, which contaminates waveforms in Figs 14 and 15, because MDD solves the inverse problem (eq. 22). As shown in Fig. 8(b), SP converted waves are weak [compare Fig. 16(c) with the other panels in Fig. 16]. Also, the slant-stacked wavefields in Figs 16(c) and (d) are more dissimilar than the wavefields in Figs 15(c) and (d) obtained by trace-by-trace cross-coherence. This is an indication that MDD successfully eliminates the crosstalk that contaminates Figs 15(c) and (d).

Leahy *et al.* (2012) show that a subhorizontal basement is located at about 3.8 km depth. The waves pointed by the three arrows in Fig. 16 are possibly reflections from the basement; their arrival times are 1.38 s (PP), 2.66 s (PS) and 4.10 s (SS). We do not pick the SP reflected wave because it has low signal-to-noise ratio. These arrival times are much larger than the estimated traveltime differences between *Pn/Sn* and *PmP/SmS*, which are 0.7 and 1.2 s. Although the differences of the traveltimes estimated by ray tracing include some uncertainties due to the subsurface model used for the ray tracing, we conclude that the retrieved waves are reflected waves but not later direct arrivals based on two reasons explained below. First, the arrival times of these reflected waves highlighted by the arrows in Fig. 16 are dependent. Using the arrival times of the PP and SS reflected waves, the arrival time of the PS reflected wave should be 2.74 s, which is a 3 per cent discrepancy [$\approx (2.74 - 2.66)/2.66$] from the observed time in Fig. 16(b). Second, the large difference of PP and SS arrival times in Fig. 16 indicates large V_p/V_s ratio, which is the condition of near surface. Therefore, the arrival times obtained from Fig. 16 include near-surface information. When we assume that the reflector is flat, the average *P* and *S* velocities over the ray paths of the reflected waves (h_r in Fig. 11) are 4.5 and 1.7 km s^{-1}, respectively, with the angles of incidence we estimated.

5 DISCUSSION OF VELOCITIES

The estimated velocities (4.2 and 1.5 km s^{-1} from direct waves, and 4.5 and 1.7 km s^{-1} from reflected waves) and velocities used for the wavefield decomposition (3.5 and 1.2 km s^{-1}) are different. These differences indicate the depth variation of velocities. Gans (2011) and Leahy *et al.* (2012) show that the velocities in the region of survey line 1 monotonically increase with depth. The velocities estimated from direct (from Fig. 12) and reflected waves (from Fig. 16) are the average velocities over the distances h_d and h_r in Fig. 11. Based on the estimated angles of incidence and the depth of the reflector, the velocities from the reflected waves include the information of deeper structure than the direct waves. Therefore, the fact that the estimated velocities from reflected waves are faster than those from direct waves is consistent with previous studies. The velocities used for decomposition are theoretically the velocities at the surface but practically the average velocities over a medium with some thickness depending on the wavelength we used. Since the velocities used for decomposition are lower than the velocities estimated from direct waves, the decomposition is sensitive for the near-surface structure shallower than the depth of $h_d \cos(\theta)$ in Fig. 11 for the used frequency range.

6 CONCLUSIONS

We apply seismic interferometry to plane waves excited by a cluster of earthquakes and obtain subsurface information on a local scale. To improve the quality of interferometric wavefields, we employ several techniques such as upgoing/downgoing *P/S* wavefield decomposition, time windowing to separate direct and reflected waves, and multidimensional analysis. The wavefield decomposition proposed here works well when the medium has no or weak lateral heterogeneity. For trace-by-trace interferometry, wavefield decomposition enhances coherence of interferometric wavefields between traces. We retrieve the Green's matrix without unwanted crosstalk of *P* and *S* waves with MDD interferometry. Although MDD interferometry requires wavefield separation, the computed waveforms follow causality and have the highest signal-to-noise ratio compared

with trace-by-trace interferometry. The difference between the velocities estimated from direct waves and reflected waves retrieved by seismic interferometry is evidence of the depth variation of the velocities.

REFERENCES

Abe, S., Kurashimo, E., Sato, H., Hirata, N., Iwasaki, T. & Kawanaka, T., 2007. Interferometric seismic imaging of crustal structure using scattered teleseismic waves, *Geophys. Res. Lett.,* **34,** L19305, doi:10.1029/2007GL030633.

Aki, K., 1957. Space and time spectra of stationary stochastic waves, with special reference to microtremors, *Bull. Earthq. Res. Inst.,* **35,** 415–456.

Aki, K. & Richards, P.G., 2002. *Quantitative Seismology,* 2nd edn, Univ. Science Books.

Assumpção, M., James, D. & Snoke, A., 2002. Crustal thicknesses in se brazilian shield by receiver function analysis: implications for isostatic compensation, *J. geophys. Res.,* **107,** ESE2–1–15.

Baig, A.M., Bostock, M.G. & Mercier, J.P., 2005. Spectral reconstruction of teleseismic P Green's functions, *J. geophys. Res.,* **110,** B08306, doi:10.1029/2005JB003625.

Bakulin, A. & Calvert, R., 2006. The virtual source method: Theory and case study, *Geophysics,* **71**(4), SI139–SI150.

Behm, M. & Shekar, B., 2014. Blind deconvolution of multichannel recordings by linearized inversion in the spectral domain, *Geophysics,* **79**(2), V33–V45.

Behm, M., Snieder, R. & Leahy, G., 2014. Retrieval of local surface velocities from traffic noise—an example from the LaBarge basin (Wyoming), *Geophys. Prospect.,* **62**(2), 223–243.

Biryol, C.B., Leahy, G.M., Zandt, G. & Beck, S.L., 2013. Imaging the shallow crust with local and regional earthquake tomography, *J. geophys. Res.,* **118,** 2289–2306.

Bostock, M.G., 2004. Green's functions, source signatures, and the normalization of teleseismic wave fields, *J. geophys. Res.,* **109,** B03303, doi:10.1029/2003JB002783.

Bostock, M.G. & Rondenay, S., 1999. Migration of scattered teleseismic body waves, *Geophys. J. Int.,* **137,** 732–746.

Bostock, M.G. & Sacchi, M.D., 1997. Deconvolution of teleseismic recordings for mantle structure, *Geophys. J. Int.,* **129,** 143–152.

Claerbout, J.F., 1968. Synthesis of a layered medium from its acoustic transmission response, *Geophysics,* **33**(2), 264–269.

Clayton, R.W. & Wiggins, R.A., 1976. Source shape estimation and deconvolution of teleseismic bodywaves, *Geophys. J. R. astr. Soc.,* **47,** 151–177.

Dankbaar, J.W.M., 1985. Separation of P- and S-waves, *Geophys. Prospect.,* **33,** 970–986.

Dasgupta, S. & Nowack, R.L., 2006. Deconvolution of three-component teleseismic P waves using the autocorrelation of the P to SV scattered waves, *Bull. seism. Soc. Am.,* **96,** 1827–1835.

Gans, C.R., 2011. Investigations of the crust and upper mantle of modern and ancient subduction zones, using Pn tomography and seismic receiver functions, *PhD thesis,* The University of Arizona.

Langston, C.A., 1979. Structure under Mount Rainier, Washington, inferred from teleseismic body waves, *J. geophys. Res.,* **84,** 4749–4762.

Leahy, G.M., Saltzer, R.L. & Schmedes, J., 2012. Imaging the shallow crust with teleseismic receiver functions, *Geophys. J. Int.,* **191,** 627–636.

Li, X., Sobolev, S.V., Kind, R., Yuan, X. & Estabrook, C., 2000. A detailed receiver function image of the upper mantle discontinuities in the japan subduction zone, *Earth planet. Sci. Lett.,* **183,** 527–541.

Loewenthal, D. & Robinson, E.A., 2000. On unified dual fields and Einstein deconvolution, *Geophysics,* **65**(1), 293–303.

Mehta, K., Bakulin, A., Sheiman, J., Calvert, R. & Snieder, R., 2007. Improving the virtual source method by wavefield separation, *Geophysics,* **72**(4), V79–V86.

Moldoveanu, N., Combee, L., Egan, M., Hampson, G., Sydora, L. & Abriel, W., 2007. Over/under towed-streamer acquisition: a method to extend seismic bandwidth to both higher and lower frequencies, *Leading Edge,* **26,** 41–58.

Nakata, N. & Snieder, R., 2012. Estimating near-surface shear-wave velocities in Japan by applying seismic interferometry to KiK-net data, *J. geophys. Res.,* **117,** B01308, doi:10.1029/2011JB008595.

Nakata, N., Snieder, R., Tsuji, T., Larner, K. & Matsuoka, T., 2011. Shear-wave imaging from traffic noise using seismic interferometry by cross-coherence, *Geophysics,* **76**(6), SA97–SA106.

Nakata, N., Snieder, R., Kuroda, S., Ito, S., Aizawa, T. & Kunimi, T., 2013. Monitoring a building using deconvolution interferometry. I. Earthquake-data analysis, *Bull. seism. Soc. Am.,* **103**(3), 1662–1678.

Pšenčík, I., 1998. Package array, version 4.10, Tech. Rep. Report 7, 403–404, Department of Geophysics, Charles University Prague.

Robertsson, J.O.A. & Curtis, A., 2002. Wavefields separation using densely deployed three-component single-sensor groups in land surface-seismic recordings, *Geophysics,* **67**(5), 1624–1633.

Robertsson, J.O.A. & Muyzert, E., 1999. Wavefield separation using a volume distribution of three componenet recordings, *Geophys. Res. Lett.,* **26**(18), 2821–2824.

Ruigrok, E., 2012. Body-wave seismic interferometry applied to earthquake- and storm-induced wavefields, *PhD thesis,* Delft University of Technology.

Ruigrok, E. & Wapenaar, K., 2012. Global-phase seismic interferometry unveils P-wave reflectivity below the Himalayas and Tibet, *Geophys. Res. Lett.,* **39,** L11303, doi:10.1029/2012GL051672.

Ruigrok, E., Campman, X., Draganov, D. & Wapenaar, K., 2010. High-resolution lithospheric imaging with seismic interferometry, *Geophys. J. Int.,* **183,** 339–357.

Ryberg, T., 2011. Body wave observations from corss-correlations of ambient seismic noise: a case study from the Karoo, RSA, *Geophys. Res. Lett.,* **38,** L13311, doi:10.1029/2011GL047665.

Schalkwijk, K.M., Wapenaar, C.P.A. & Verschuur, D.J., 2003. Adaptive decomposition of multicomponent ocean-bottom seismic data into downgoing and upgoing P- and S-waves, *Geophysics,* **68**(3), 1091–1102.

Schmedes, J., Roth, J.B., Saltzer, R.L. & Leahy, G.M., 2012. Imaging the shallow crust using teleseismic tomography, *Bull. seism. Soc. Am.,* **102**(3), 1276–1282.

Snieder, R. & Şafak, E., 2006. Extracting the building response using seismic interferometry: theory and application to the Millikan Library in Pasadena, California, *Bull. seism. Soc. Am.,* **96**(2), 586–598.

Snieder, R., Sheiman, J. & Calvert, R., 2006. Equivalence of the virtual-source method and wave-field deconvolution in seismic interferometry, *Phys. Rev. E,* **73,** 066620.

Snieder, R., Miyazawa, M., Slob, E., Vasconcelos, I. & Wapenaar, K., 2009. A comparison of strategies for seismic interferometry, *Surv. Geophys.,* **30**(10), 503–523.

Tonegawa, T., Nishida, K., Watanabe, T. & Shiomi, K., 2009. Seismic interferometry of teleseismic S-wave coda retrieval of body waves: an application to the Philippine Sea slab underneath the Japanese Islands, *Geophys. J. Int.,* **178,** 1574–1586.

van der Neut, J. & Bakulin, A., 2009. Estimating and correcting the amplitude radiation pattern of a virtual source, *Geophysics,* **74**(2), SI27–SI36.

van der Neut, J., Tatanova, M., Thorbecke, J., Slob, E. & Wapenaar, K., 2011a. Deghosting, demultiple, and deblurring in controlled-source seismic interferometry, *Int. J. Geophys.,* **2011,** 870819, doi:10.1155/2011/870819.

van der Neut, J., Thorbecke, J., Mehta, K., Slob, E. & Wapenaar, K., 2011b. Controlled-source interferometric redatuming by crosscorrelation and multidimensional deconvolution in elastic media, *Geophysics,* **76**(4), SA63–SA76.

Vasconcelos, I. & Snieder, R., 2008a. Interferometry by deconvolution. Part 1—theory for acoustic waves and numerical examples, *Geophysics,* **73**(3), S115–S128.

Vasconcelos, I. & Snieder, R., 2008b. Interferometry by deconvolution. Part 2—theory for elastic waves and application to drill-bit seismic imaging, *Geophysics,* **73**(3), S129–S141.

Vasconcelos, I., Snieder, R. & Hornby, B., 2008. Imaging internal multiples from subsalt VSP data—examples of target-oriented interferometry, *Geophysics,* **73**(4), S157–S168.

Wapenaar, C.P.A., Herrmann, P., Verschuur, D.J. & Berkhout, A.J., 1990. Decomposition of multicomponent seismic data into primary P- and S-wave responses, *Geophys. Prospect.,* **38,** 633–661.

Wapenaar, K., 2004. Retrieving the elastodynamic Green's function of an arbitrary inhomogeneous medium by cross correlation, *Phys. Rev. Lett.,* **93,** 254301, doi:10.1103/PhysRevLett.93.254301.

Wapenaar, K., Slob, E. & Snieder, R., 2008a. Seismic and electromagnetic controlled-source interferometry in dissipative media, *Geophys. Prospect.,* **56,** 419–434.

Wapenaar, K., van der Neut, J. & Ruigrok, E., 2008b. Passive seismic interferometry by multidimensional deconvolution, *Geophysics,* **73**(6), A51–A56.

Wapenaar, K., Draganov, D., Snieder, R., Campman, X. & Verdel, A., 2010a. Tutorial on seismic interferometry. Part 1—basic principles and applications, *Geophysics,* **75**(5), 75A195–75A209.

Wapenaar, K., Slob, E., Snieder, R. & Curtis, A., 2010b. Tutorial on seismic interferometry. Part 2—underlying theory and new advances, *Geophysics,* **75**(5), 75A211–75A227.

Wapenaar, K., Ruigrok, E., van der Neut, J. & Draganov, D., 2011a. Improved surface-wave retrieval from ambient seismic noise by multi-dimensional deconvolution, *Geophys. Res. Lett.,* **38,** L01313, doi:10.1029/2010GL045523.

Wapenaar, K., van der Neut, J., Ruigrok, E., Draganov, D., Hunziker, J., Slob, E., Thorbecke, J. & Snieder, R., 2011b. Seismic interferometry by crosscorrelation and by multidimensional deconvolution: a systematic comparison, *Geophys. J. Int.,* **185,** 1335–1364.

Yang, Z., Sheehan, A.F., Yeck, W.L., Miller, K.C., Erslev, E.A., Worthington, L.L. & Harder, S.H., 2012. Imaging basin structure with teleseismic virtual source reflection profiles, *Geophys. Res. Lett.,* **39,** L02303, doi:10.1029/2011GL050035.

APPENDIX A: WAVEFIELD DECOMPOSITION WHEN $U_p = 0$ OR $U_s = 0$

In this appendix, we show that we can use eq. (11) for wavefield decomposition even if $U_p(k, \omega) = 0$ or $U_s(k, \omega) = 0$ at a specific wavenumber and frequency. This condition may exist when incoming waves contain only a limited range of plane waves, and the horizontal wavenumbers in direct upgoing P and S waves are different (e.g. the earthquake data in this study). When $U_s(k, \omega) = 0$, we can express $D_s(k, \omega)$ as

$$D_s(k, \omega) = \frac{\omega^2 - 2\beta^2 k^2}{\beta \omega v_s} u_x(k, 0, \omega) = -\frac{2\beta k}{\omega} u_z(k, 0, \omega)$$

$$= \frac{\omega^2 - 2\beta^2 k^2}{2\beta \omega v_s} u_x(k, 0, \omega) - \frac{\beta k}{\omega} u_z(k, 0, \omega) \qquad (A1)$$

from eqs (5), (6), (9) and (10). Note that eq. (A1) is valid only for limited wavenumbers and frequencies where $U_s(k, \omega) = 0$. The last equality in eq. (A1) is the same as the expression for $D_s(k, \omega)$

in eq. (11). Therefore, we can decompose $D_s(k, \omega)$ from observed wavefields even when $U_s(k, \omega) = 0$. When we insert eq. (A1) into eqs (9) and (10) with $U_s(k, \omega) = 0$, we obtain

$$U_p(k, \omega) - D_p(k, \omega) = \frac{-\beta(k^2 - v_s^2)}{2\alpha k v_p} D_s$$

$$= -\frac{\omega^2 - 2\beta^2 k^2}{\alpha \omega v_p} u_z(k, 0, \omega), \qquad (A2)$$

$$U_p(k, \omega) + D_p(k, \omega) = \frac{2\beta^3 k v_s}{\alpha(\omega^2 - 2\beta^2 k^2)} D_s = \frac{2\beta^2 k}{\alpha \omega} u_x(k, 0, \omega). \qquad (A3)$$

By adding/subtracting eqs (A2) and (A3), we derive the same expressions as in eq. (11) for upgoing/downgoing P waves. When $U_p(k, \omega) = 0$,

$$D_p(k, \omega) = \frac{2\beta^2 k}{\alpha \omega} u_x(k, 0, \omega) = -\frac{\omega^2 - 2\beta^2 k^2}{2\alpha \omega v_p} u_z(k, 0, \omega)$$

$$= \frac{\beta^2 k}{\alpha \omega} u_x(k, 0, \omega) + \frac{\omega^2 - 2\beta^2 k^2}{2\alpha \omega v_p} u_z(k, 0, \omega), \qquad (A4)$$

and hence we can use the same expressions for computing downgoing P and upgoing/downgoing S waves as shown in eq. (11).